Postprint of: Balcerzak, D., Szpunar, I., Strandbakke, R., Saeed, S. W., Bazioti, C., Mielewczyk-Gryń, A., Winiarz, P., Carrillo, A., Balaguer, M., Serra, J. M., Gazda, M., & Wachowski, S. (2023). Oxide nanoparticle exsolution in Lu-doped (Ba,La)CoO3. CRYSTENGCOMM, 25, 4306-4316. https://doi.org/10.1039/d3ce00422h

Oxide nanoparticle exsolution in Lu-doped (Ba,La)CoO_3

Daria Balcerzak[1], Iga Szpunar[1], Ragnar Strandbakke[2], Sarmad W. Saeed[2], Calliope Bazioti[3], Aleksandra Mielewczyk-Gryń[1], Piotr Winiarz[4], Alfonso J. Carrillo[5], María Balaguer[5], Jose M. Serra[5], Maria Gazda[1], Sebastian Wachowski[1]

[1] Institute of Nanotechnology and Materials Engineering, Faculty of Applied Physics and Mathematics, and Advanced Materials Centre, Gdańsk University of Technology, Gdańsk, Poland

[2] Department of Chemistry, Centre for Materials Science and Nanotechnology, University of Oslo, 0371 Oslo, Norway

[3] Department of Physics, Centre for Materials Science and Nanotechnology, University of Oslo, 0371 Oslo, Norway

[4] Department of Hydrogen Energy, Faculty of Energy and Fuels, AGH University of Science and Technology, Kraków, Poland

[5] Instituto de Tecnología Química, Universitat Politècnica de València-Consejo Superior de Investigaciones Científicas, Avenida Los Naranjos s/n, 46022 Valencia, Spain

Abstract:

This study investigated Lu doping of $Ba_{0.5}La_{0.5}CoO_3$ and its influence on the exsolution of oxide nanoparticles (NPs). As a result of Lu doping, we observed the phase segregation into the main $Ba_{0.4}La_{0.6}Co_{0.85}Lu_{0.15}O_3$ (BLCO-Lu) phase and the secondary $Ba_{0.85}La_{0.15}Co_{0.75}Lu_{0.25}O_3$ (BCO-Lu) phase. We noticed the exsolution of BCO-Lu nanoparticles on the main BLCO-Lu phase. Moreover, the BLCO-Lu phase exsolved in the form of nanoparticles on the adjacent BCO-Lu grains. That shows that the phases are covered with mutually exsolved oxide NPs. In addition, trace amounts of the $BaLuCo_4O_7$ phase are detected. We noticed that the exsolved oxides even in the as-prepared sample were fine (average size of 18 nm), and well distributed with a dense population of NPs above 280 per 1 μm^2. Furthermore, we showed that the size and shape of the exsolved oxide NPs can be controlled by varying the annealing temperature. For example, at 800 °C the exsolved oxides segregate and form two different shapes; spherical and cuboidal, with an average size of 31 nm and NPs population of about 23 NPs/μm^2. Meanwhile, with lowering the temperature to 400 °C the oxides form only spherical and quite evenly distributed NPs with the occurrence of 137 NPs per 1 μm^2. The obtained results open the possibility of tailoring a novel, more catalytically active material for future applications in electrochemical devices.

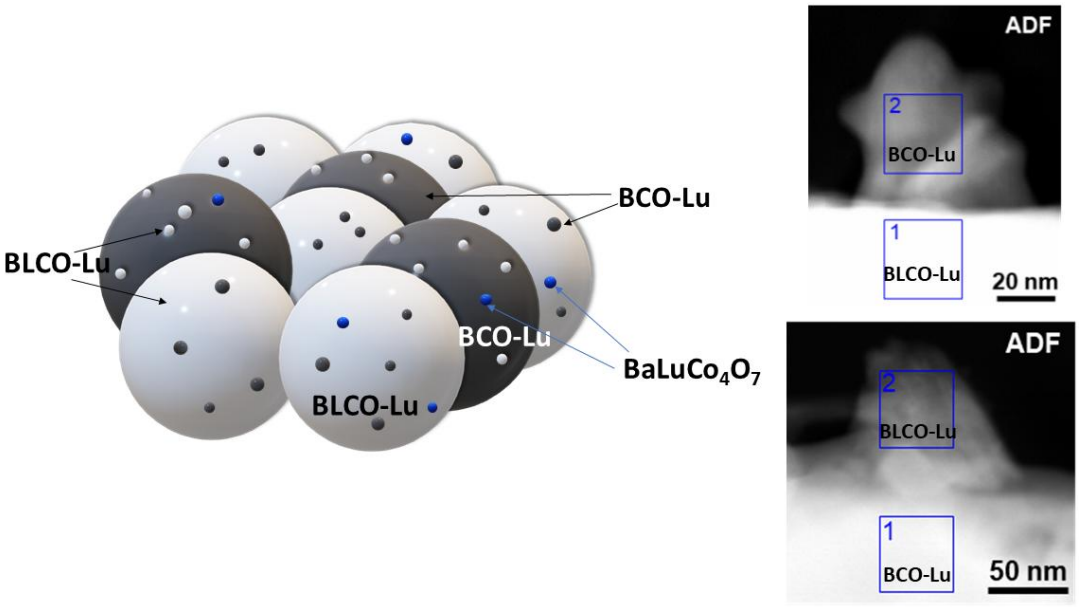

Keywords: cobaltites, Lu substitution, oxide exsolution

1. Introduction

Exsolution is a process for the fabrication of well-dispersed metal or metal oxide nanoparticles (NPs) on a parent oxide surface that has attracted great attention in recent years [1,2]. This is because the exsolution process has a fundamental advantage over other nanoparticle deposition or infiltration techniques – the exsolved nanoparticles are anchored on the surface, preventing coarsening and agglomeration [3–5]. The nanoparticle anchoring is the result of the nanoparticle emergence from cations contained in the oxide crystal lattice that under certain conditions (reducing atmospheres for metallic NPs) migrate to the oxide surface. The external forces driving exsolution are mainly thermal processing [6], but also voltage [7–9], plasma [10], or light [11] can be applied. In addition, control over exsolution can be gained by adjusting several varieties of intrinsic factors. They include doping one of the host lattices, for example, with other transition metals [10], the introduction of cation deficiency or excess [12], lattice strain [13], or oxygen non-stoichiometry [3][12,14]. It should be noted that exsolution has a wide area of applications, thanks to the possibilities of designing different advanced nanostructures [15]. For example, it may be applied to modify anode materials in solid-oxide [14][16–18], and protonic ceramic electrochemical cells [19], materials used in water and carbon dioxide (co)electrolysis [20], methane conversion into ethylene [21], photocatalysis [22], gas sensing [23], or hydrocarbon reforming [24–26]. In these studies, it has been demonstrated that surface functionalization with exsolved nanoparticles increase the material's catalytic activity with high stability over prolonged operation [27,28].

So far, most studies have been devoted to metal nanoparticle exsolution mechanisms. It involves the nucleation and growth of a metal NP on the surface of ceramic grains, which occurs generally in a reducing atmosphere [29]. For example, in the case of the $La_{0.43}Ca_{0.37}Ti_{0.94}Ni_{0.06}O_3$ perovskite, Ni nanoparticles were released from the host lattice as a result of thermal treatment in hydrogen, resulting in evenly distributed nanosized metal particles [10].

The exsolution of oxide nanoparticles has also been reported [30–32], but to a lesser extent, and still, many aspects of this process are uncovered. It is noted that oxide nanoparticles can be formed under an oxidizing atmosphere, which significantly spreads the possibilities of their application [30][33]. So far, few reports of successful exsolution of CoO [30], and MnO [31] have been published. It was observed that by changing the temperature and oxygen partial pressure, different forms of cobalt oxide are exsolved on the surface [30]. The exsolution of cobalt oxide on the surface of non-stoichiometric $Ca_3Co_4O_{9-\delta}$ oxides was also presented. It was shown that their presence and size may be tuned through annealing time and the sample nonstoichiometry [34]. Rioja-Monllor and co-workers [33] applied exsolution for the preparation of the 0.4 $La_{0.8}Ba_{0.2}CoO_{3-\delta}$–0.6 $BaZr_{0.6}Co_{0.4}O_{3-\delta}$ nanocomposite, illustrating that such a modification of the proton ceramic fuel cell cathode resulted in low area-specific resistance at low temperature. On the other hand, Zhao et al. reported the exsolution of the BaO, SrO and Fe whiskers on the $Ba_{0.3}Sr_{0.7}Fe_{0.9}Mn_{0.1}O_{3-\delta}$ anode [17]. The presence of more complex oxide nanoparticles, such as $BaCoO_{3-\delta}$ (BCO) on the $PrBa_{0.8}Ca_{0.2}Co_2O_{5+\delta}$ surface [35][36], $Gd_xCo_yO_{3-\delta}$ on the $Ba_{0.8}Gd_{0.8-x}Pr_{0.4}Co_{2-y}O_{5+\delta}$ surface [37] was also reported. Though several works have been published, the mechanism of oxide nanoparticle exsolution is still insufficiently investigated. That points to the necessity of carrying out exsolution studies which will help to understand how different factors, especially the temperature, influence the exsolution of oxide nanoparticles.

In recent years, perovskites with the general formula $BaLnCo_2O_6$ (Ln - lanthanide) or their derivatives gained interest thanks to their interesting properties. They show high electronic conductivity [38–42] and some of them also have proton conductivity [38,39]. Moreover, owing to multiple polymorph variants it is possible to tune their properties by structural modifications [38][43]. Further modifications via exsolution allow the development of these materials by improving their surface properties. For instance, the nanoparticles exsolved on the surface of an electrode, as active, anchored sites for reactions with the surrounding atmosphere may provide stable long-term performance of electrochemical devices [37].

This work presents the exsolution of cobalt oxide nanoparticles on the surface of $Ba_{0.5}La_{0.5}CoO_3$–based perovskites. Two types of ~~o~~xides were exsolved, that is, $Ba_{0.4}La_{0.6}Co_{0.85}Lu_{0.15}O_{3-\delta}$ and $Ba_{0.85}La_{0.15}Co_{0.75}Lu_{0.25}O_{3-\delta}$. We show how the population, size and chemical composition of nanoparticles can be controlled by adjusting the thermal treatment. We believe that our results will help in expanding the knowledge of the oxide exsolution mechanism, enabling a fine tune of the properties of multifunctional composites.

2. Experimental route:

2.1. Synthesis and sample preparation

The applied experimental procedure is summarized in Figure 1. Samples of $Ba_{0.5}La_{0.4}Lu_{0.1}CoO_3$ were synthesized using a conventional solid-state reaction. The stoichiometric amounts of La_2O_3 (pre-annealed for 5 h at 950 °C, 99.9% Alfa Aesar), Lu_2O_3 (99.9%, Chempur), $BaCO_3$ (99.9% Sigma Aldrich), and Co_3O_4 (99.98% Alfa Aesar) were ball milled using Planetary ball mill Fritsch Pulverisette 7 Classic Line in isopropanol in 20 hour-long cycles. The cycle consisted of 50 min milling with 450 RPM speed and 10 min pause. The mass ratio of milling media (5 mm diameter zirconia balls) to reagent mass was 5:1. The slurry was then dried, and the resultant powder was

uniaxially pressed into pellets (217 MPa). The green bodies were sintered at 1200 °C for 48 hours in ambient air with a heating/cooling rate of 3 °C/min.

The as-synthesized pellets were examined in terms of their structural and microstructural properties. Then, the samples were subjected to further thermal treatment to investigate the influence of the annealing temperature on the nanoparticle exsolution. Five samples were heated with a 3 °C/min ramp to a temperature from the range of 400 – 1200 °C (with a 200 °C step). After 20 h of annealing the samples were quenched, that is, they were quickly removed from the tube furnace and placed into a beaker filled with room-temperature water.

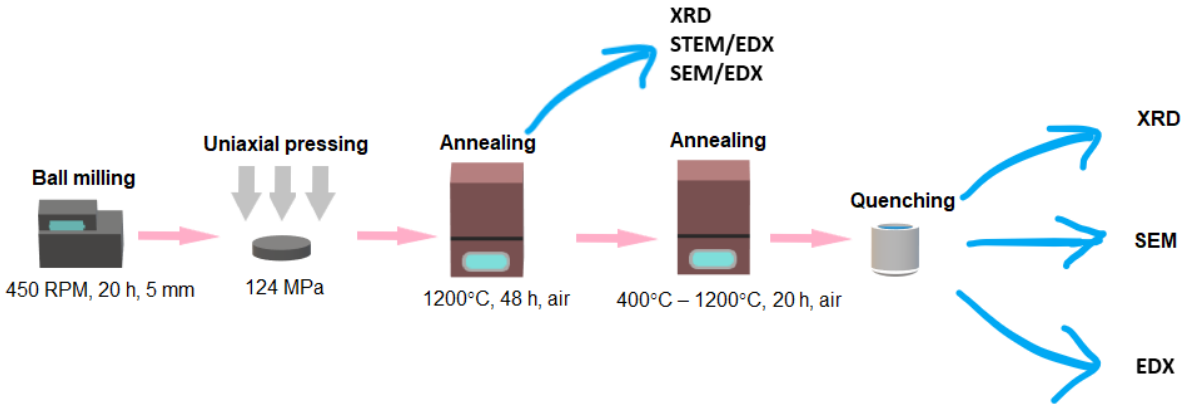

FIGURE 1 Diagram of the solid-state reaction synthesis of the compound and further thermal treatment.

2.2. Characterisation

The crystal structure of analysed materials was characterised using a Phillips X'Pert Pro X-ray diffractometer at room temperature with Cu K_α radiation. The HighScore Plus software [44] was used to identify the phase composition of each sample.

The Rietveld refinement was carried out using GSAS-II software [45] to determine structural parameters and phase fractions. The following structures were used as initial models for the analysis: cubic $Ba_{0.5}La_{0.5}CoO_3$ (space group $Pm\bar{3}m$, no. 221, ID number 00-032-0480 from ICDD PDF [46]), $BaCoO_{2.22}$ (space group $Pm\bar{3}m$, no. 221, ID number 7033669 from COD, 2015 [47]) and $BaLuCo_4O_7$ (space group $P3_1c$, no. 159, ID 01-073-9255 ICDD PDF [46].

The microstructure and elemental composition of the samples were investigated using a FEI Quanta FEG 250 scanning electron microscope (SEM) with EDAX Apollo energy dispersive spectrometer (EDX). The microstructural analysis of exsolved nanoparticles requires both the highest possible resolution and phase contrast sensitivity, therefore two modes were used to obtain micrographs. To obtain micrographs with the highest resolution Secondary Electron (SE) signal was collected with Everhart-Thornley Detector (ETD). The experiment was conducted in the high vacuum mode and 20 kV acceleration voltage was used. In this mode, EDX analysis of selected points and areas of the specimen was performed. In order to increase the number of EDX counts and expand the energy spectrum, the acceleration voltage during spectra collection was increased to 30 kV. For the same sample regions as the ones scanned for the high-resolution micrographs, another experiment was performed to collect phase contrast micrographs with a relatively high resolution. An electron field immersion mode was applied, which

means that the acceleration voltage was reduced to 5 kV and a reverse bias of 4 kV between the sample stage and the column was applied. As a result, the electron landing energy was reduced to 1 keV, and the bias accelerated BSE upwards to a "low Voltage high Contrast Detector" (vCD), mounted coaxially on the beam column exit. The vCD collects Back-Scattered Electrons (BSE) and the immersion is used to maximize the signal, which results in phase-sensitive images with a resolution of ~ 20 nm.

The average size of the exsolved nanoparticles was measured with the use of ImageJ software based on SEM images. In addition, the nanoparticle surface density describing the population of nanoparticles, and the mean standard deviation were calculated.

Scanning transmission electron microscopy (STEM) investigations were conducted on an FEI Titan G2 60-300 kV equipped with a CEOS DCOR probe-corrector and Super-X EDX detectors. Observations were performed at 300 kV with a probe convergence angle of 24 mrad. The camera length was set at 60 mm and simultaneous STEM imaging was conducted with 3 detectors: high-angle annular dark-field (HAADF) (collection angles 101.7–200 mrad), ADF (collection angles 22.4–101.7 mrad), and annular bright-field (ABF) (collection angles 8.5–22.4 mrad). The resulting spatial resolution achieved was approximately 0.08 nm. Energy-dispersive X-ray spectroscopy (EDX) was applied to identify the chemical composition of the samples. For the STEM-EDX studies, the samples were previously ground in a mortar into powders and applied on Cu-grids supported by holey-C films. Plasma cleaning was applied before the STEM investigations with a Fishione Model 1020.

3. Results and discussion

3.1. Structural and phase composition analysis

Our initial assumption was that Lu-substitution on the A-site of the $Ba_{0.5}La_{0.5}CoO_3$ perovskite, because of the size mismatch, would introduce strain serving as a driving force for further exsolution of oxide nanoparticles. As shown in Figure 2, instead of the single-phase $Ba_{0.5}La_{0.4}Lu_{0.1}CoO_3$ oxide, a composite material formed consisting of three phases. The most intensive XRD reflections were identified as corresponding to two cubic ($Pm\bar{3}m$ space group) perovskites. The main perovskite phase, denoted as BLCO-Lu, is isostructural with $Ba_{0.5}La_{0.5}CoO_3$, whereas the second one, denoted as BCO-Lu, has been indexed as the $BaCoO_{3-\delta}$ perovskite. The third phase was assigned to $BaLuCo_4O_7$ with the hexagonal $P6_3mc$ space group, which is consistent also with the trigonal $P3_1c$ space group, a maximal non-isomorphic subgroup of the $P6_3mc$ symmetry [48].

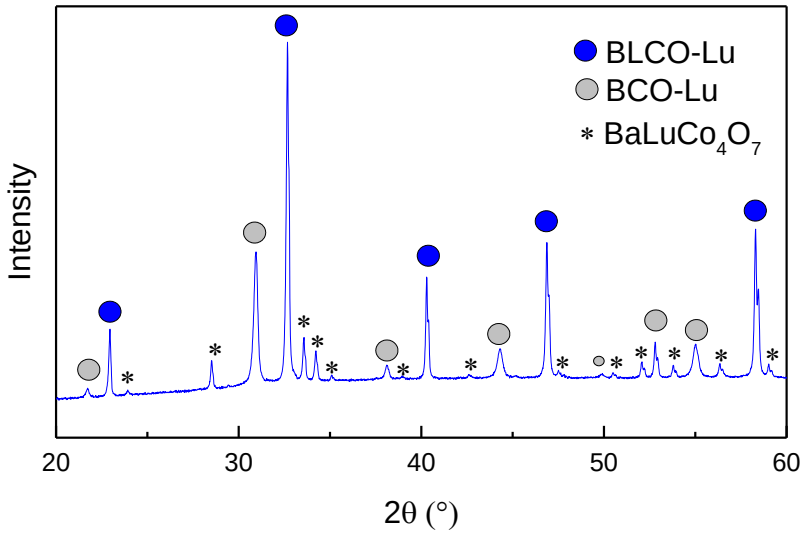

FIGURE 2 The XRD pattern of the as-synthesized sample with the reflections of identified phases marked.

To assist phase identification, STEM with EDX investigations were performed. Various areas were scanned, and EDX data indicated the existence of two phases (for an exemplary result see Figure 6). The third phase was not found in the STEM experiment since it is a local technique by which minority phases may be not detected. In both observed phases, the overall ratio of metal cation to oxygen anion content was close to 40:60 at. %, which is characteristic of perovskites. The average compositions of two phases identified by STEM/EDX analysis performed in several grains are Ba 7 at. %, La 12 at. %, Lu 3 at. % and Co 17 at. % and Ba 17 at. %, La 3 at. %, Lu 5 at. % and Co 15 at. %. This indicates that their compositions are $Ba_{0.4}La_{0.6}Co_{0.85}Lu_{0.15}O_{3-\delta}$ and $Ba_{0.85}La_{0.15}Co_{0.75}Lu_{0.25}O_{3-\delta}$, which indicates that they are the BLCO-Lu and BCO-Lu perovskite phases determined by XRD. The Goldschmidt tolerance parameter values of BLCO-Lu (0.91) and BCO-Lu (0.94) calculated using the compositions determined by STEM/EDX are consistent with the cubic perovskite structure. In both phases, Lu occupies the B-site rather than the A-site. To further analyse whether Lu could reside in the A-site in $Ba_{0.5}La_{0.5}CoO_3$, an additional experiment was performed. We have attempted to synthesize samples with the nominal compositions of $Ba_{0.5}La_{0.475}Lu_{0.025}CoO_{3-\delta}$, $Ba_{0.5}La_{0.485}Lu_{0.015}CoO_{3-\delta}$ and $Ba_{0.5}La_{0.495}Lu_{0.005}CoO_{3-\delta}$. The results, presented in SI **(***cf.* SI Figure S1 and Table S1) showed that even for as low as 0.5 mol. % Lu content, a two-phase material composed of BLCO-Lu and BCO-Lu was obtained. Thus, regardless of the content of Lu, obtaining a single-phase material by the solid-state synthesis method seems not possible.

Structural analysis of the ceramics was performed using Rietveld refinement analysis. The compositions of the BLCO-Lu and BCO-Lu phases were constrained according to the STEM results, i.e. $Ba_{0.4}La_{0.6}Co_{0.85}Lu_{0.15}O_{3-\delta}$ and $Ba_{0.85}La_{0.15}Co_{0.75}Lu_{0.25}O_{3-\delta}$, respectively. An exemplary graphical presentation of the refinement results is presented in Figure 3 a), whereas the unit cell parameters and weight phase fractions are collected in SI Table S2.

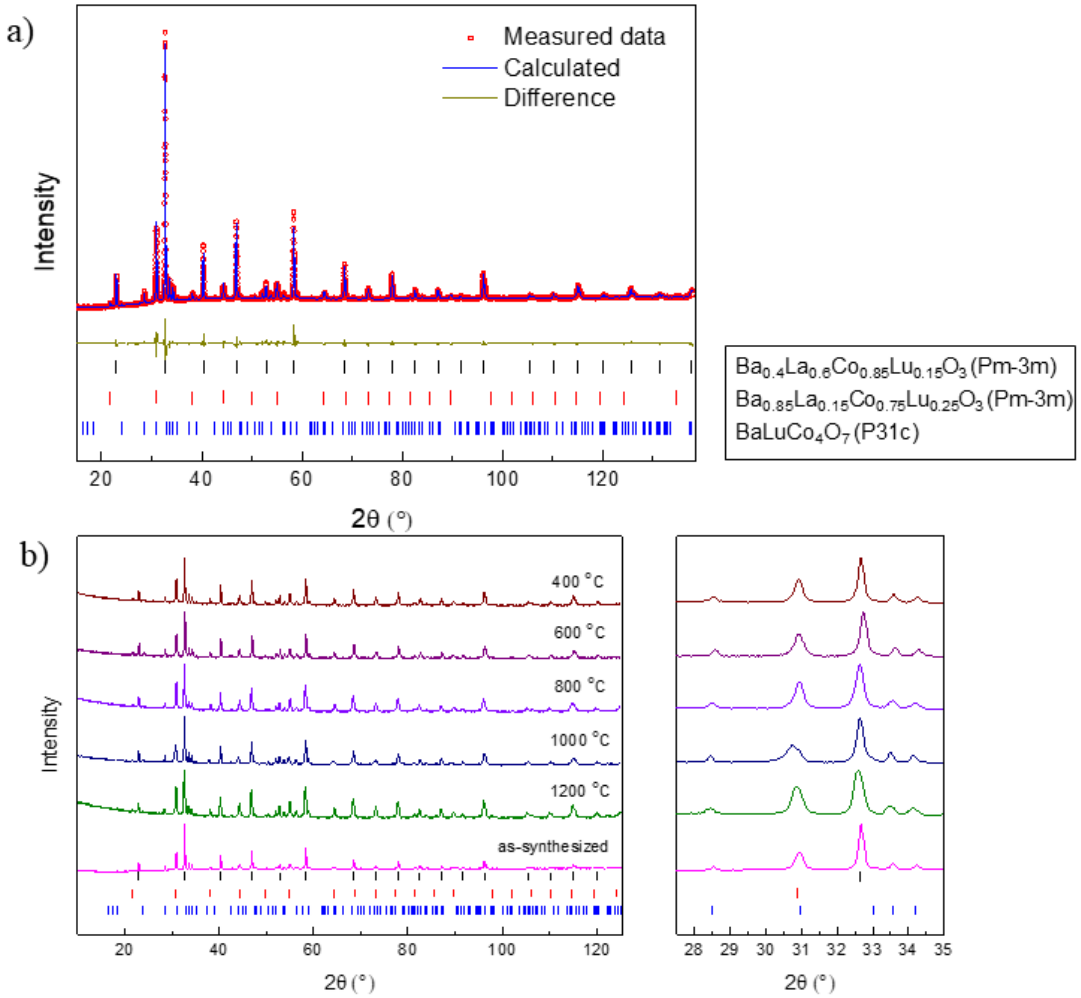

FIGURE 3 a) The representative Rietveld refinement profiles of as-synthesized powder (R_w = 1.89%, R_e = 0.96%). The data points are marked by red circles, the refined pattern is a solid blue line. The difference between measured and calculated data is shown in the difference plot, below the refined pattern. Bragg positions of each phase are presented by vertical bars at the bottom, b) X-ray diffraction patterns of as-synthesized and annealed at different temperature samples with Bragg positions of each phase. On the right, the magnification of the 27.5° – 35° angle range of the X-ray pattern is shown.

Since in the specimen annealed at 600 °C the growth of the third phase was the most promoted and elongated crystals partially covering the surface were observed, this sample was excluded from the analysis of the nanometric exsolution. The description of the microstructure and chemical composition of this sample can be found in SI in Section 2. *Investigation of sample annealed at 600 °C*. The investigation of phase composition as a function of annealing temperature for the samples annealed below 600 °C was evaluated by SEM with EDX measurements. In this study, we combine BSE imaging in immersion mode, to maximize both resolution and phase contrast, with SEM with EDX data analysis. The results are presented in Figure 4.

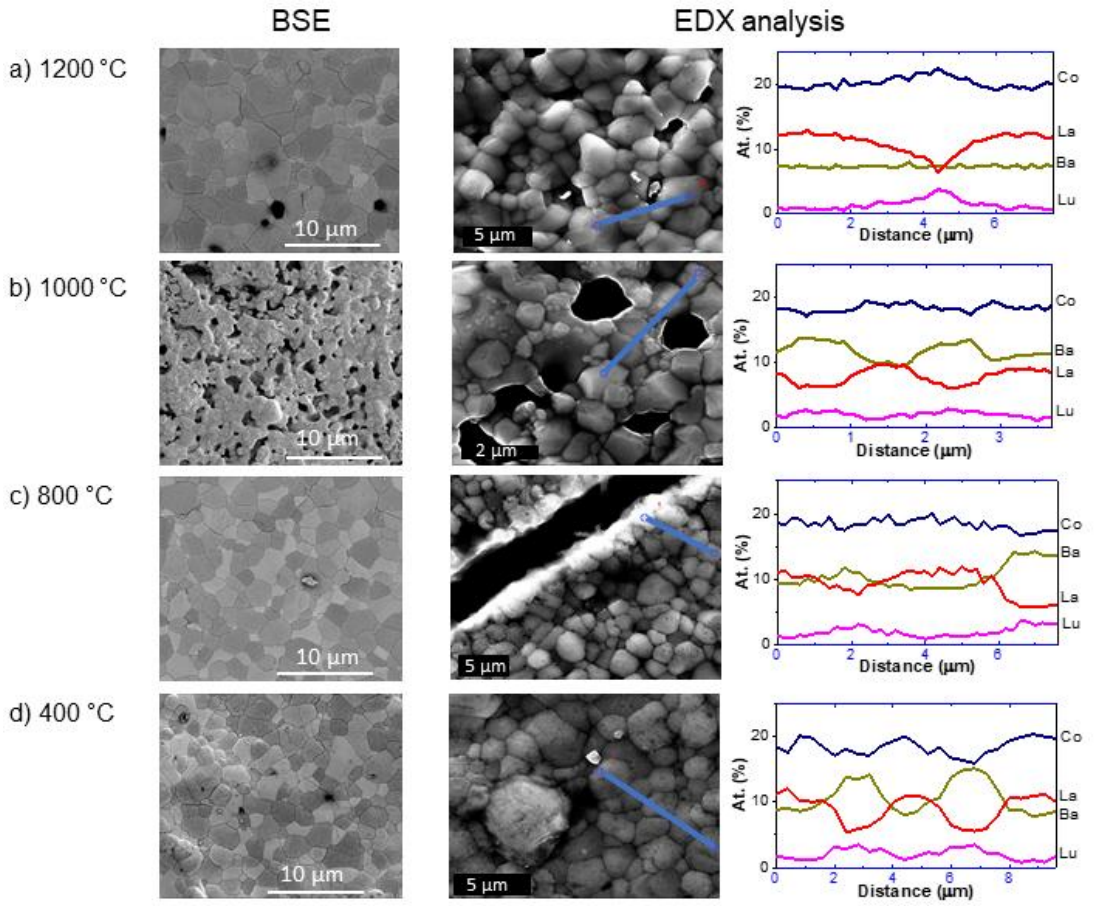

FIGURE 4 SEM images of the samples annealed at a) 1200 °C, b) 1000 °C, c) 800 °C and d) 400 °C obtained in the immersion mode with BSE signal (vCD detector) and with EDX line scans based on SEM images in SE mode.

The SEM micrographs show that all samples except the one annealed at 1000 °C have similar microstructure. They are dense, and polycrystalline with some isolated pores. The analysis obtained by BSE imaging and EDX studies confirmed the difference in phase composition in adjacent grains. The adjacent grains show phase contrast, in which bright and dark grains are visible. The change in contrast is related to differences in the average elemental mass in the volume of each grain, which is 4.5 and 4.0 $u\,x\,Å^{-3}$, respectively, for BLCO-Lu and BCO-Lu. Therefore, the brighter grains should correspond to the main BLCO-Lu phase, while the darker to the BCO-Lu secondary phase. The presence of differentiation in the composition is also confirmed by EDX analysis. The EDX line scan measurements along the grains were performed in the same areas as the BSE studies. The line scans were set to be long enough to visualize the composition of several grains. For each sample, grains of different compositions are observed. There are ones with the composition corresponding to BLCO-Lu, and another to the BCO-Lu phase. In addition, individual grains consisting of the $BaLuCo_4O_7$ were detected during SEM imaging with EDX analysis (*cf.* SI Fig. S2 for additional EDX results).

The sample annealed at 1000 °C is different from the others. It is porous, shows the uniformity of the composition in the BSE image and smaller differences in composition between grains are indicated by the EDX analysis. In addition, it was

observed that large crystals were formed in isolated spots on the sample surface. The EDX analysis revealed that they are composed mostly of barium carbonate and their size reached hundreds of micrometres (*cf.* SI Figure S4 for further EDX analysis). The barium carbonate crystals formed between the annealing and the SEM analysis. This implies that prolonged annealing at this temperature leads to the formation of a metastable material, which can partially decompose at RT.

3.2.Exsolution analysis by high-resolution microscopy

High-resolution secondary electron SEM micrographs of the as-synthesized sample are presented in Figure 5. The surface of the sample is covered by spherical and longitudinal nanoparticles with a size of up to 35 nm, with the average size of the nanoparticles about 18 nm. The nanoparticle size distribution is presented in Fig. 5 c). The exsolved nanoparticles are abundant (280 particles μm^{-2}) and distributed quite uniformly on the surface, with a slight population increase in the vicinity of the grain boundary. In addition, slight variations of nanoparticle population can be observed on different grains. Further STEM with EDX analysis is provided to identify the nanoparticle composition, and on which types of grains they are formed.

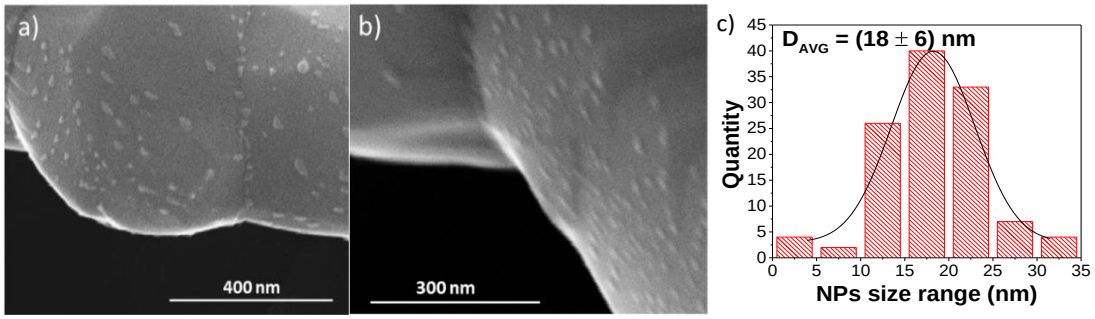

FIGURE 5 The as-prepared sample a) SEM micrographs under magnification of 150 000 and b) 200 000x obtained in SE mode (ETD detector), c) NPs size distribution based on a) SEM micrograph.

The results of STEM-EDX of the as-synthesized sample are presented in Figure 6. They confirm the differentiation in chemical composition. In the first studied region (Figure 6 a - b), the large crystal grain (Area 1) has a composition close to the BLCO-Lu phase, whereas the exsolved particle consists predominantly of barium and cobalt. That indicates that the chemical formula of the nanoparticle is BCO-Lu. The other area analysed by STEM-EDX (Figure 6 c – d) shows the opposite. The larger grain exhibits a higher content of barium, and cobalt, which is indicative of the BCO-Lu phase, while the nanoparticle has the composition of the BLCO-Lu phase. In both cases, the exsolved nanoparticles comply with the general composition of ABO_3 perovskite. Moreover, lutetium is substituted on the cobalt site of each exsolved oxide nanoparticle, which was exposed by STEM/EDX measurements. Based on the chemical composition analysis the nanoparticles exsolved on the adjacent grains differ. Namely, the BCO-Lu nanoparticles are formed on BLCO-Lu, and the opposite BLCO-Lu are formed on BCO-Lu. Additional elemental EDX analysis of another sample region, presented in Figure 6 e), confirms this conclusion. It can be observed that, in the boundary between the substrate and the exsolved particle, the chemical composition rapidly changes: the content of lanthanum drops, whereas these of lutetium and barium is increased.

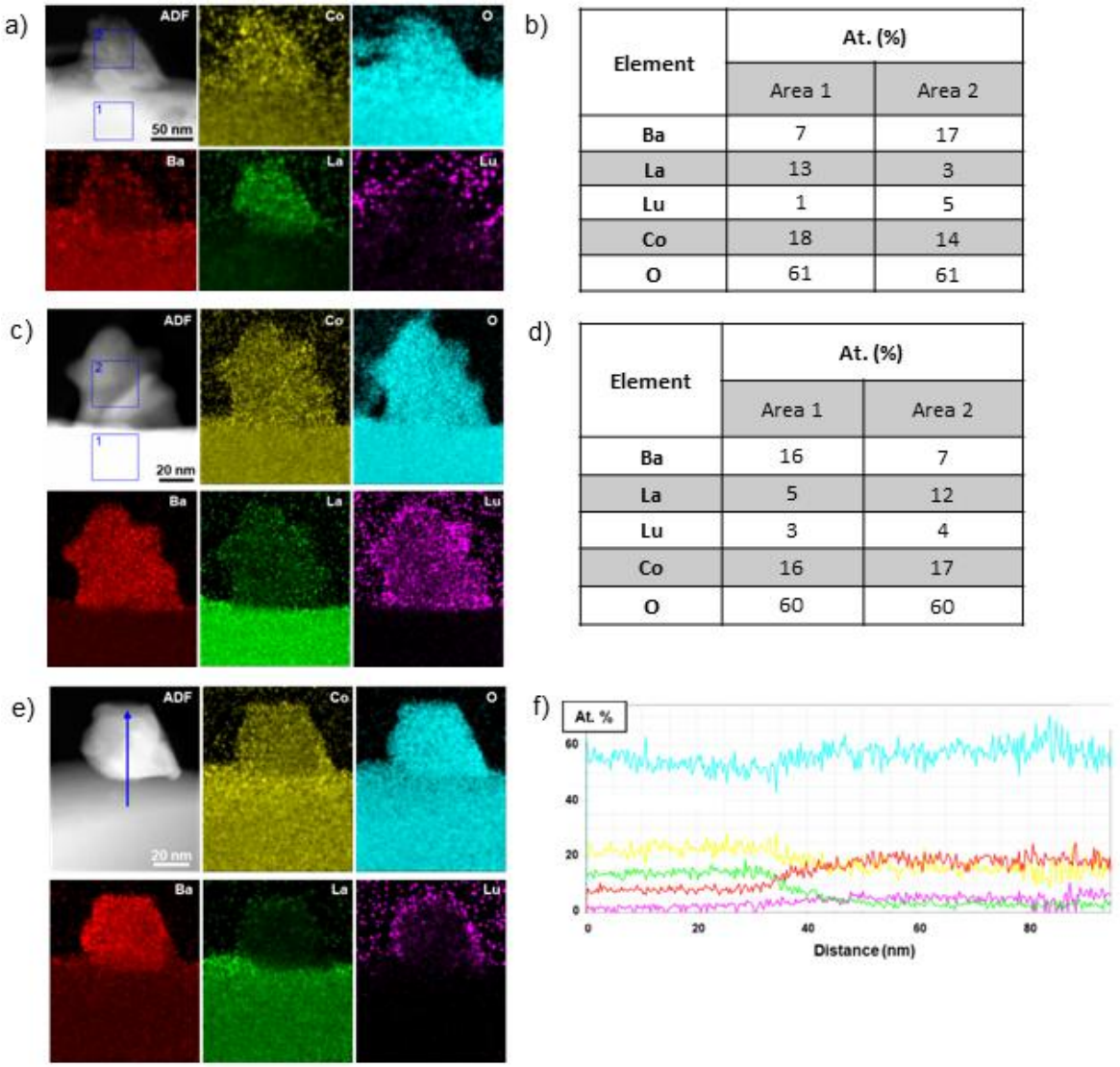

Element	At. (%)	
	Area 1	Area 2
Ba	7	17
La	13	3
Lu	1	5
Co	18	14
O	61	61

Element	At. (%)	
	Area 1	Area 2
Ba	16	7
La	5	12
Lu	3	4
Co	16	17
O	60	60

FIGURE 6 STEM-EDX quantified maps of as-synthesized sample and corresponding chemical composition of marked areas: 1 – substrate, and 2 – exsolved nanoparticle. (a-b) and (e) BCO-Lu nanoparticle exsolved on BLCO-Lu substrate, (c-d) BLCO-Lu nanoparticle exsolved on BCO-Lu substrate. In (e) STEM image with f) EDX line scan profiles clearly show the abrupt change in the chemical composition when crossing the boundary between substrate and the exsolved nanoparticle: the content of La drops, whereas the content of Lu and Ba is increased.

To evaluate the influence of the heat treatment on nanoparticle formation, further SEM studies of the annealed specimens were performed and summarized in Figure 7. It is observed that, at the highest annealing temperature (1200 °C), exsolved nanoparticles are small (average NPs size around 27 nm) and spherical (Fig. 7 a), with a tendency to grow along the grain boundaries (see SI Figure S5). Moreover, cracks appear in the specimen with the edges covered with nanoparticles. The average size of NPs is twice as large as in the as-prepared specimen and their number decrease significantly after annealing from 280 to 28 NPs per μm^2. It is observed that NPs are not uniformly distributed unlike in the as-prepared specimen. The BSE investigation shows that nanoparticles are exsolved on each grain (presented also in SI Figure S5).

In the sample annealed at 1000 °C, shown in Figure 7 b), the nanoparticles were not detected. The analysis shows only sub-micron grains. The BSED analysis showed that

they are probably BCO-Lu. The presence of relatively small crystallites of BCO-Lu in the sample annealed at 1000 °C is also observed through the broadening of the XRD reflections. The full width at half maximum (FWHM) of the main peak for BCO-Lu phase of the sample annealed at 1000 °C is about 0.45° while for the as-synthesized sample, it equals 0.27°. This indicates that 1000 °C is not appropriate to exsolve nanoparticles in this compound, because it promotes growth of large barium carbonate and smaller BCO-Lu crystals.

The lower annealing temperature, 800 °C, which corresponds to the image shown in Figure 7 c), enables to exsolve different types of nanoparticles. The first group of small (average size of 31 nm) and spherical nanoparticles is similar to those obtained at 1200 °C, whereas the second group comprises larger rectangular-shaped particles growing at the grain boundaries. The NPs population at that temperature achieves the value of 23 NPs/μm^2. In the BSED scan (SI Figure S6) the exsolved nanoparticles show a difference in contrast from the substrate. As shown before, the adjacent grains exhibit phase contrast. It is seen that the spherical nanoparticles are exsolved evenly on brighter grains, thus on the BLCO-Lu phase. The larger, cuboidal nanoparticles are growing at the boundaries, on the side of these brighter grains. The composition of exsolved phase can be attributed to the BCO-Lu phase. It is consistent with the XRD results which show a slight increase in that phase content with respect to as-prepared specimen (in SI, Table S2). The grains with a darker shade of grey, the BCO-Lu phase, do not show nanoparticles which indicates that the exsolution of BLCO-Lu does not occur at this temperature.

On the surface of the sample annealed at 400 °C (Figure 7 d) the highest number of nanoparticles, i.e. approximately 137 NPs/μm^2, is observed. In this sample, the exsolution occurs on both types of grains, which is shown in SI in Figure S7. The observed NPs are fine and spherical with an average size of around 37 nm, similarly to those obtained at 1200 °C. Nanoparticles are evenly distributed on the grains and do not grow larger at the grain boundaries as seen at, for e.g. 800 °C.

The NP population, and their average size, collected for all samples with exsolved NPs, are presented in Figure 7 e) and Figure 7 f), respectively. In comparison to as-prepared sample further annealing decreases the population of NPs at each temperature. It leads also to an increase in the average NPs size, which may point to two processes occurring during annealing. One is a further growth of the nanoparticles which were already exsolved on the as-prepared surface. Another possible process is the dissolution of NPs on selected grains depending on the annealing temperature. Thus, the final size and number of NPs is directly related to the annealing temperature determining the ultimate characteristics of NPs.

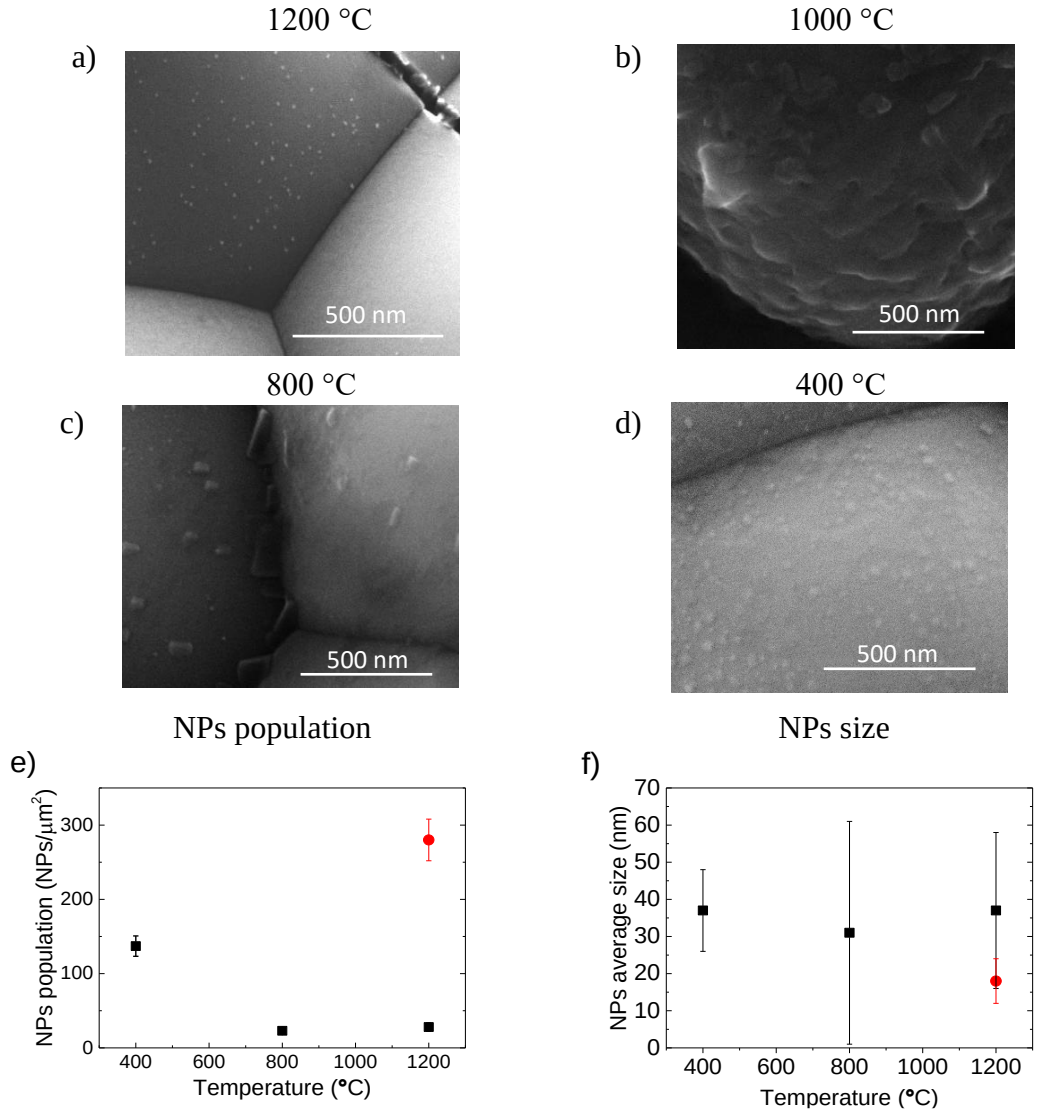

FIGURE 7 a) – d) SEM images of annealed specimen obtained in SE mode, and e) NPs population and f) NPs average size as a function of the heat-treatment temperature. Black squares correspond to the annealed specimen and red dot to the as-prepared.

In summary, the results of this study show that the nanoparticles are formed both at the BLCO-Lu main phase and the BCO-Lu secondary phase. Cooling after synthesis was not sufficiently slow to equilibrate the phase composition and microstructure at each temperature. So that they reflect a state corresponding to a temperature somewhere at the point below, which diffusion is too slow to allow thermodynamic equilibrium during cooling. Annealing at the highest temperature – 1200 °C – leads to re-equilibration between all phases, therefore the secondary phase content of BCO-Lu increases, while the number of nanoparticles decreases. At 1000 °C nanoparticles were not observed and the grains of BCO-Lu are of submicron-size, which suggests that at this temperature nanoparticles of BCO-Lu which were formed in the as-received sample, grown. At 800 °C the nanoparticles are formed exclusively on the grains of the main phase BLCO-Lu. Further decrease of the annealing temperature to 400 °C does not change the microstructure with respect to the as-prepared sample, and the population of nanoparticles is higher compared to other annealing temperatures. Any further thermal treatment followed by quenching finally reduces the NPs population relative to the as-prepared

specimen. This suggests that the exsolution of oxide nanoparticles occurs during relatively slow cooling of the sample between the synthesis temperature (1200 °C) and room temperature, what differs the most from the metallic exsolution, which does not occur in synthesized specimen under oxidizing conditions.

Finally, the overall analysis of this study suggests that upon proper heat treatment and sample preparation, the Lu-doped $BaCoO_3$ nanoparticles exsolution is a viable option in $BaLnCo_2O_6$. These cobaltites in general exhibit superb electrode performance [39–41], and it has been shown that $BaCoO_3$ is a good catalyst and improves cathodic operation in fuel cells [49,50]. A combination of these two features shows great promise in the improvement of materials proposed to be more efficient in, for example, high-temperature electrochemical cells, such as fuel cells or steam electrolysers.

4. Conclusions

$Ba_{0.5}La_{0.5}CoO_3$ doped with Lu was synthesized to analyse the exsolution of oxide nanoparticles on the surface of this material. The structural analysis results showed that Lu is preferably incorporated into the B-site cation sublattice of perovskites. The obtained ceramics were composed of two cubic perovskites (BLCO-Lu and BCO-Lu) and a lower than 6% amount of $BaLuCo_4O_7$. The compositions of the BLCO-Lu and BCO-Lu phases were found to be $Ba_{0.4}La_{0.6}Co_{0.85}Lu_{0.15}O_{3-\delta}$ and $Ba_{0.85}La_{0.15}Co_{0.75}Lu_{0.25}O_{3-\delta}$, respectively.

As a result of exsolution, two types of nanoparticles formed on the surface. The BCO-Lu nanoparticles formed on the BLCO-Lu crystal grains, and conversely, the BLCO-Lu nanoparticles formed on the BCO-Lu grains. It was proposed that the exsolution of oxide nanoparticles occurs during relatively slow cooling of the sample between the synthesis temperature and room temperature. We can conclude that this behaviour differs from the metallic particle exsolution, where in as-synthesized sample the metallic NPs do not appear on the surface.

An annealing at temperatures in the range 400 °C – 1200 °C followed by quenching was performed to observe the effect of temperature on the microstructure and nanoparticle formation. It was found that this thermal treatment reduced the NPs population and increased their size relative to the as-prepared specimen. These were explained by the growth of the nanoparticles and their dissolution on selected grains depending on the annealing temperature.

Based on our studies on the oxide exsolution, it is possible to obtain exsolved NPs under oxidizing conditions and additionally tailor their characteristics, and hence material properties, through adjusting the parameter of annealing temperature. This work presents also the ability to synthesize $BaLnCo_2O_6$ material with exsolved catalytically active $BaCoO_3$ nanoparticles doped with Lu. This carries great promise for the development of more catalytically active materials in a wide spectrum of applications.

Acknowledgements:

Project FunKeyCat is supported by the National Science Centre, Poland under the M-ERA.NET 2, which has received funding from the European Union's Horizon 2020 research and innovation program under grant agreement no 685451. The Research Council of Norway is also acknowledged for support to the Norwegian Center for Transmission Electron Microscopy (NORTEM) (no. 197405/F50).

References:

[1] J. Zhang, M.R. Gao, J.L. Luo, In Situ Exsolved Metal Nanoparticles: A Smart Approach for Optimization of Catalysts, Chem. Mater. 32 (2020) 5424–5441. https://doi.org/10.1021/acs.chemmater.0c00721.

[2] K. Kousi, C. Tang, I.S. Metcalfe, D. Neagu, Emergence and Future of Exsolved Materials, Small. 17 (2021). https://doi.org/10.1002/smll.202006479.

[3] H. Uğuz, A. Goyal, T. Meenpal, I.W. Selesnick, R.G. Baraniuk, N.G. Kingsbury, A. Haiter Lenin, S. Mary Vasanthi, T. Jayasree, M. Adam, E.Y.K. Ng, S.L. Oh, M.L. Heng, Y. Hagiwara, J.H. Tan, J.W.K. Tong, U.R. Acharya, G. Cappiello, S. Das, E.B. Mazomenos, K. Maharatna, G. Koulaouzidis, J. Morgan, P.E. Puddu, M.A. Goda, P. Hajas, G.D. Clifford, C. Liu, B. Moody, D. Springer, I. Silva, Q. Li, R.G. Mark, D. Kristomo, R. Hidayat, I. Soesanti, A. Kusjani, I. Grzegorczyk, M. Solinski, M. Lepek, A. Perka, J. Rosinski, J. Rymko, K. Stepien, J. Gieraltowski, A. Ghaffari, M.R. Homaeinezhad, M. Khazraee, M.M. Daevaeiha, J. Xu, L.G. Durand, P. Pibarot, S.K. Randhawa, M. Singh, J. Robinson, K. Xi, R.V. Kumar, A.C. Ferrari, H. Au, M.-M. Titirici, A. Parra Puerto, A. Kucernak, S.D.S. Fitch, N. Garcia-Araez, J. Herzig, A. Bickel, A. Eitan, N. Intrator, J. Robinson, K. Xi, R.V. Kumar, A.C. Ferrari, H. Au, M.-M. Titirici, A. Parra Puerto, A. Kucernak, S.D.S. Fitch, N. Garcia-Araez, H. Search, C. Journals, A. Contact, M. Iopscience, I.P. Address, A.M. Rahman, T.A. Manuscript, I.O.P. Publishing, A. Manuscript, A. Manuscript, C.C. By-nc-nd, A. Manuscript, C. Liu, D. Springer, G.D. Clifford, D. verma Atul, and Y.H. Lei Shao, Qing Gao, Xie, Jianzhong Fu, Meixiang Xiang, E. Kay, A. Agarwal, M. Gjoreski, A. Gradisek, B. Budna, M. Gams, G. Poglajen, H. Li, Y. Ren, G. Zhang, R. Wang, J. Cui, W. Zhang, A.K. Dwivedi, S.A. Imtiaz, E. Rodriguez-Villegas, Review on exsolution and its driving forces in perovskites To, J. Phys. Energy. 2 (2020) 0–31.

[4] D. Neagu, V. Kyriakou, I.L. Roiban, M. Aouine, C. Tang, A. Caravaca, K. Kousi, I. Schreur-Piet, I.S. Metcalfe, P. Vernoux, M.C.M. Van De Sanden, M.N. Tsampas, In Situ Observation of Nanoparticle Exsolution from Perovskite Oxides: From Atomic Scale Mechanistic Insight to Nanostructure Tailoring, ACS Nano. 13 (2019) 12996–13005. https://doi.org/10.1021/acsnano.9b05652.

[5] Y. Gao, Z. Lu, T.L. You, J. Wang, L. Xie, J. He, F. Ciucci, Energetics of Nanoparticle Exsolution from Perovskite Oxides, J. Phys. Chem. Lett. 9 (2018) 3772–3778. https://doi.org/10.1021/acs.jpclett.8b01380.

[6] J. Tan, D. Lee, J. Ahn, B. Kim, J. Kim, J. Moon, Thermally driven in situ exsolution of Ni nanoparticles from (Ni, Gd)CeO2 for high-performance solid oxide fuel cells, J. Mater. Chem. A. 6 (2018) 18133–18142. https://doi.org/10.1039/c8ta05978k.

[7] J.H. Myung, D. Neagu, D.N. Miller, J.T.S. Irvine, Switching on electrocatalytic activity in solid oxide cells, Nature. 537 (2016) 528–531. https://doi.org/10.1038/nature19090.

[8] G. Tsekouras, D. Neagu, J.T.S. Irvine, Step-change in high temperature steam electrolysis performance of perovskite oxide cathodes with exsolution of B-site dopants, Energy Environ. Sci. 6 (2013) 256–266.

https://doi.org/10.1039/c2ee22547f.

[9] A. Nenning, A.K. Opitz, C. Rameshan, R. Rameshan, R. Blume, M. Hävecker, A. Knop-Gericke, G. Rupprechter, B. Klötzer, J. Fleig, Ambient pressure XPS study of mixed conducting perovskite-type SOFC cathode and anode materials under well-defined electrochemical polarization, J. Phys. Chem. C. 120 (2016) 1461–1471. https://doi.org/10.1021/acs.jpcc.5b08596.

[10] O. Kwon, S. Joo, S. Choi, S. Sengodan, G. Kim, Review on exsolution and its driving forces in perovskites, JPhys Energy. 2 (2020). https://doi.org/10.1088/2515-7655/ab8c1f.

[11] Y. Lu, Q. Shen, Q. Yu, F. Zhang, G. Li, W. Zhang, Photoinduced in situ growth of ag nanoparticles on AgNbO3, J. Phys. Chem. C. 120 (2016) 28712–28716. https://doi.org/10.1021/acs.jpcc.6b10961.

[12] D. Neagu, G. Tsekouras, D.N. Miller, H. Ménard, J.T.S. Irvine, In situ growth of nanoparticles through control of non-stoichiometry, Nat. Chem. 5 (2013) 916–923. https://doi.org/10.1038/nchem.1773.

[13] H. Han, J. Park, S.Y. Nam, K.J. Kim, G.M. Choi, S.S.P. Parkin, H.M. Jang, J.T.S. Irvine, Lattice strain-enhanced exsolution of nanoparticles in thin films, Nat. Commun. 10 (2019) 1–8. https://doi.org/10.1038/s41467-019-09395-4.

[14] Y. Gao, D. Chen, M. Saccoccio, Z. Lu, F. Ciucci, From material design to mechanism study: Nanoscale Ni exsolution on a highly active A-site deficient anode material for solid oxide fuel cells, Nano Energy. 27 (2016) 499–508. https://doi.org/10.1016/j.nanoen.2016.07.013.

[15] D. Neagu, V. Kyriakou, I.L. Roiban, M. Aouine, C. Tang, A. Caravaca, K. Kousi, I. Schreur-Piet, I.S. Metcalfe, P. Vernoux, M.C.M. Van De Sanden, M.N. Tsampas, In Situ Observation of Nanoparticle Exsolution from Perovskite Oxides: From Atomic Scale Mechanistic Insight to Nanostructure Tailoring, ACS Nano. 13 (2019) 12996–13005. https://doi.org/10.1021/acsnano.9b05652.

[16] B. Hua, M. Li, Y.F. Sun, J.H. Li, J.L. Luo, Enhancing Perovskite Electrocatalysis of Solid Oxide Cells Through Controlled Exsolution of Nanoparticles, ChemSusChem. 10 (2017) 3333–3341. https://doi.org/10.1002/cssc.201700936.

[17] J. Zhao, Y. Pu, L. Li, W. Zhou, Y. Guo, Efficient Ferrite-Based Perovskite Anode for Solid Oxide Fuel Cells with A-Site and B-Site Co-exsolution, Energy and Fuels. 34 (2020) 10100–10108. https://doi.org/10.1021/acs.energyfuels.0c02140.

[18] J. Li, B. Wei, X. Yue, L. Zhe, A Highly Efficient and Robust Perovskite Anode with Iron–Palladium Co-exsolutions for Intermediate-Temperature Solid-Oxide Fuel Cells, ChemSusChem. 11 (2018) 2593–2603. https://doi.org/10.1002/cssc.201800641.

[19] C. Duan, R.J. Kee, H. Zhu, C. Karakaya, Y. Chen, S. Ricote, A. Jarry, E.J. Crumlin, D. Hook, R. Braun, N.P. Sullivan, R. O'Hayre, Highly durable, coking and sulfur tolerant, fuel-flexible protonic ceramic fuel cells, Nature. 557 (2018) 217–222. https://doi.org/10.1038/s41586-018-0082-6.

[20] V. Kyriakou, D. Neagu, E.I. Papaioannou, I.S. Metcalfe, M.C.M. van de Sanden, M.N. Tsampas, Co-electrolysis of H2O and CO2 on exsolved Ni nanoparticles for efficient syngas generation at controllable H2/CO ratios, Appl. Catal. B Environ. 258 (2019) 117950. https://doi.org/10.1016/j.apcatb.2019.117950.

[21] C. Zhu, S. Hou, X. Hu, J. Lu, F. Chen, K. Xie, Electrochemical conversion of methane to ethylene in a solid oxide electrolyzer, Nat. Commun. 10 (2019) 1–8. https://doi.org/10.1038/s41467-019-09083-3.

[22] Y.F. Sun, Y.L. Yang, J. Chen, M. Li, Y.Q. Zhang, J.H. Li, B. Hua, J.L. Luo, Toward a rational photocatalyst design: A new formation strategy of co-catalyst/semiconductor heterostructures: Via in situ exsolution, Chem. Commun. 54 (2018) 1505–1508. https://doi.org/10.1039/c7cc08797g.

[23] D. Wang, D. Zhang, Q. Mi, A high-performance room temperature benzene gas sensor based on CoTiO3 covered TiO2 nanospheres decorated with Pd nanoparticles, Sensors Actuators B Chem. 350 (2022) 130830. https://doi.org/10.1016/j.snb.2021.130830.

[24] D. Zubenko, S. Singh, B.A. Rosen, Exsolution of Re-alloy catalysts with enhanced stability for methane dry reforming, Appl. Catal. B Environ. 209 (2017) 711–719. https://doi.org/10.1016/j.apcatb.2017.03.047.

[25] A.J. Carrillo, K.J. Kim, Z.D. Hood, A.H. Bork, J.L.M. Rupp, La0.6Sr0.4Cr0.8Co0.2O3Perovskite Decorated with Exsolved Co Nanoparticles for Stable CO2 Splitting and Syngas Production, ACS Appl. Energy Mater. 3 (2020) 4569–4579. https://doi.org/10.1021/acsaem.0c00249.

[26] A.J. Carrillo, L. Navarrete, M. Laqdiem, M. Balaguer, J.M. Serra, Boosting methane partial oxidation on ceria through exsolution of robust Ru nanoparticles, Mater. Adv. 2 (2021) 2924–2934. https://doi.org/10.1039/d1ma00044f.

[27] D. Neagu, T.S. Oh, D.N. Miller, H. Ménard, S.M. Bukhari, S.R. Gamble, R.J. Gorte, J.M. Vohs, J.T.S. Irvine, Nano-socketed nickel particles with enhanced coking resistance grown in situ by redox exsolution, Nat. Commun. 6 (2015). https://doi.org/10.1038/ncomms9120.

[28] Q.A. Islam, S. Paydar, N. Akbar, B. Zhu, Y. Wu, Nanoparticle exsolution in perovskite oxide and its sustainable electrochemical energy systems, J. Power Sources. 492 (2021) 229626. https://doi.org/10.1016/j.jpowsour.2021.229626.

[29] B.A. Rosen, Progress and Opportunities for Exsolution in Electrochemistry, Electrochem. 1 (2020) 32–43. https://doi.org/10.3390/electrochem1010004.

[30] D.S. Tsvetkov, I.L. Ivanov, D.A. Malyshkin, A.Y. Zuev, Oxygen content, cobalt oxide exsolution and defect structure of the double perovskite PrBaCo2O6-δ, J. Mater. Chem. A. 4 (2016) 1962–1969. https://doi.org/10.1039/c5ta08390g.

[31] S. Sengodan, Y.W. Ju, O. Kwon, A. Jun, H.Y. Jeong, T. Ishihara, J. Shin, G. Kim, Self-Decorated MnO Nanoparticles on Double Perovskite Solid Oxide Fuel Cell Anode by in Situ Exsolution, ACS Sustain. Chem. Eng. 5 (2017) 9207–9213. https://doi.org/10.1021/acssuschemeng.7b02156.

[32] A.M. Arévalo-López, M. Huvé, P. Simon, O. Mentré, The hidden story in BaNiO 3 to BaNiO 2 transformation: Adaptive structural series and NiO exsolution, Chem. Commun. 55 (2019) 3717–3720. https://doi.org/10.1039/c8cc09610d.

[33] L. Rioja-Monllor, C. Bernuy-Lopez, M.L. Fontaine, T. Grande, M.A. Einarsrud, Processing of high performance composite cathodes for protonic ceramic fuel cells by exsolution, J. Mater. Chem. A. 7 (2019) 8609–8619. https://doi.org/10.1039/c8ta10950h.

[34] K.S. Roy, C. Subramaniam, L.S. Panchakarla, Non-Stoichiometry Induced Exsolution of Metal Oxide Nanoparticles via Formation of Wavy Surfaces and their Enhanced Electrocatalytic Activity: Case of Misfit Calcium Cobalt Oxide, ACS Appl. Mater. Interfaces. 13 (2021) 9897–9907. https://doi.org/10.1021/acsami.0c20891.

[35] J.H. Kim, S. Yoo, R. Murphy, Y. Chen, Y. Ding, K. Pei, B. Zhao, G. Kim, Y.M. Choi, M. Liu, Promotion of oxygen reduction reaction on a double perovskite electrode by a water-induced surface modification, Energy Environ. Sci. 14 (2021) 1506–1516. https://doi.org/10.1039/d0ee03283b.

[36] Y. Zhou, E. Liu, Y. Chen, Y. Liu, L. Zhang, W. Zhang, Z. Luo, N. Kane, B. Zhao, L. Soule, Y. Niu, Y. Ding, H. Ding, D. Ding, M. Liu, An Active and Robust Air Electrode for Reversible Protonic Ceramic Electrochemical Cells, ACS Energy Lett. 6 (2021) 1511–1520. https://doi.org/10.1021/acsenergylett.1c00432.

[37] F. Zhu, F. He, D. Liu, H. Zhang, Y. Xu, K. Xu, Y. Chen, A surface reconfiguration of a perovskite air electrode enables an active and durable reversible protonic ceramic electrochemical cell, Energy Storage Mater. 53 (2022) 754–762. https://doi.org/https://doi.org/10.1016/j.ensm.2022.10.009.

[38] S. Wachowski, I. Szpunar, M. Sorby, A. Mielewczyk-Gryń, M. Balaguer, C. Ghica, M.C. Istrate, M. Gazda, A.E. Gunnæs, J.M. Serra, T. Norby, R. Strandbakke, Structure and water uptake in BaLnCo2O6-δ (Ln =La, Pr, Nd, Sm, Gd, Tb and Dy), Acta Mater. Under Revi (2020). https://doi.org/10.1016/j.actamat.2020.08.018.

[39] R. Strandbakke, V.A. Cherepanov, A.Y. Zuev, D.S. Tsvetkov, C. Argirusis, G. Sourkouni, S. Prünte, T. Norby, Gd- and Pr-based double perovskite cobaltites as oxygen electrodes for proton ceramic fuel cells and electrolyser cells, Solid State Ionics. 278 (2015) 120–132. https://doi.org/10.1016/j.ssi.2015.05.014.

[40] E. Vøllestad, R. Strandbakke, M. Tarach, D. Catalán-Martínez, M.L. Fontaine, D. Beeaff, D.R. Clark, J.M. Serra, T. Norby, Mixed proton and electron conducting double perovskite anodes for stable and efficient tubular proton ceramic electrolysers, Nat. Mater. 18 (2019) 752–759. https://doi.org/10.1038/s41563-019-0388-2.

[41] S. Choi, C.J. Kucharczyk, Y. Liang, X. Zhang, I. Takeuchi, H. Il Ji, S.M. Haile, Exceptional power density and stability at intermediate temperatures in protonic ceramic fuel cells, Nat. Energy. 3 (2018) 202–210. https://doi.org/10.1038/s41560-017-0085-9.

[42] I. Szpunar, S. Wachowski, T. Miruszewski, K. Dzierzgowski, K. Górnicka, T. Klimczuk, M.H. Sørby, M. Balaguer, J.M. Serra, R. Strandbakke, M. Gazda, A. Mielewczyk-Gryń, Electric and magnetic properties of lanthanum barium cobaltite, J. Am. Ceram. Soc. 103 (2020) 1809–1818. https://doi.org/10.1111/jace.16865.

[43] I. Szpunar, R. Strandbakke, M.H. Sørby, S.L. Wachowski, M. Balaguer, M. Tarach, J.M. Serra, A. Witkowska, E. Dzik, T. Norby, M. Gazda, A. Mielewczyk-Gryń, High-temperature structural and electrical properties of BaLnCo2O6 positrodes, Materials (Basel). 13 (2020) 1–18. https://doi.org/10.3390/ma13184044.

[44] T. Degen, M. Sadki, E. Bron, U. König, G. Nénert, The high score suite, Powder Diffr. 29 (2014) S13–S18. https://doi.org/10.1017/S0885715614000840.

[45] B.H. Toby, R.B. Von Dreele, GSAS-II: The genesis of a modern open-source all purpose crystallography software package, J. Appl. Crystallogr. 46 (2013) 544–549. https://doi.org/10.1107/S0021889813003531.

[46] S. Gates-Rector, T. Blanton, The Powder Diffraction File: a quality materials characterization database, Powder Diffr. 34 (2019) 352–360. https://doi.org/10.1017/S0885715619000812.

[47] S. Graulis, D. Chateigner, R.T. Downs, A.F.T. Yokochi, M. Quirós, L. Lutterotti, E. Manakova, J. Butkus, P. Moeck, A. Le Bail, Crystallography Open Database - An open-access collection of crystal structures, J. Appl. Crystallogr. 42 (2009) 726–729. https://doi.org/10.1107/S0021889809016690.

[48] W. Wong-Ng, W. Xie, Y. Yan, G. Liu, J. Kaduk, E. Thomas, T. Tritt, Structural and thermoelectric properties of BaRCo 4O 7 (R = Dy, Ho, Er, Tm, Yb, and Lu), J. Appl. Phys. 110 (2011). https://doi.org/10.1063/1.3663526.

[49] Y. Chen, S. Yoo, W. Zhang, J.H. Kim, Y. Zhou, K. Pei, N. Kane, B. Zhao, R. Murphy, Y. Choi, M. Liu, Effective Promotion of Oxygen Reduction Reaction by in Situ Formation of Nanostructured Catalyst, ACS Catal. 9 (2019) 7137–7142. https://doi.org/10.1021/acscatal.9b01738.

[50] K. Pei, Y. Zhou, Y. Ding, K. Xu, H. Zhang, W. Yuan, K. Sasaki, Y.M. Choi, M. Liu, Y. Chen, An improved oxygen reduction reaction activity and CO2-tolerance of La0.6Sr0.4Co0.2Fe0.8O3-δ achieved by a surface modification with barium cobaltite coatings, J. Power Sources. 514 (2021) 230573. https://doi.org/10.1016/j.jpowsour.2021.230573.